Methods for Monitoring 3-D Temperature Distributions in Power Electronic Modules

Christoph H. van der Broeck*,**, Robert D. Lorenz** and Rik W. De Doncker*
*Institute for Power Electronics and Electrical Drives (ISEA), RWTH Aachen University
Jaegerstrasse 17-19, 52066 Aachen, Germany, Email: post@isea.rwth-aachen.de
** Wisconsin Electric Machines and Power Electronics Consortium (WEMPEC), University of Wisconsin-Madison
1415 Engineering Drive, 53706 Madison, WI, Email: rdlorenz@wisc.edu

***Abstract*—In this paper, an observer for spatial temperature estimation within power electronic modules is presented. It estimates the junction temperature of the power devices as well as at material interconnects within the power module with high bandwidth. These temperatures can then be monitored to estimate the damage caused by thermomechanical cycling, or even to manipulate cycles by thermal control. The observer is based on a static and dynamic loss model and a transient thermal model. The thermal real time model is derived from a 3-D finite difference model by balanced truncation, such that it can be computed on a conventional digital signal processor. Based on the models and device temperature information, a cascaded observer structure is proposed. It estimates the transient and averaged temperature spatially at various locations of the power module with nearly zero lag, even if the sensor information exhibits delays and has noisy signals. This zero lag, 3-D estimation has not been achieved in prior work Experimental results demonstrate the feasibility and performance of the proposed observer structure.**

***Index Terms* - Thermal Observer, Real Time Model, Thermal Model, Loss Model, Model Truncation, IGBT, Power Electronics**

I. Introduction

The replacement of combustion engines by electrical drives in automobiles is a world-wide trend. Every year more new models are introduced to the market and the technology is becoming more mature. As a result, a strong competition is about to rise about how to make the electrical drive train, in particular the power module, smaller and cheaper.

In this development, dynamic thermal monitoring of power modules is a critical tool [1]. It allows the operation of the devices close to their thermal limit [2] or even enables active thermal cycles reduction [3]–[6]. In addition, the temperature estimates can be used for condition monitoring e.g. to detect delamination of interconnects within the module [1], [7]. This allows limiting the maximum permissible stress, such that further degradation can be reduced and there is a sufficient time left to bring the vehicle to maintenance.

Over the last decade, some very promising concepts for thermal observers have been introduced and analyzed [3], [8]–[11]. A computational efficient junction temperature estimator has been proposed in [11]. It provides an inexpensive and effective solution. However, it does not allow incorporating information from a temperature sensor. A classical Luenberger-style thermal observer has been realized with a 1-D Cauer model in [9] and its performance was demonstrated experimentally. In [8], it was shown how a classical observer structure can be enhanced by using an adaptive model to incorporate changes of the coolant flow rate. A very important property of observer structures is illustrated in [10] and [12]. It discusses how temperature sensitive electrical parameters, in this particular case the forward voltage of the device, can be effectively combined with an observer for high bandwidth junction temperature estimation.

However, the introduced concepts have certain drawbacks, which must be addressed. All classical closed loop Luenberger-style thermal observer, which were used in [8]–[10], [12], do not provide zero steady-state estimation error, as they only rely on proportional feedback paths. To overcome this problem an enhanced-Luenberger-style observer concept can be used, which has been proposed in [3]. In addition to the proportional feedback-paths, it uses an integral observer state feedback path, which results in zero steady-state error.

The thermal models used in all presented thermal observer structures were one dimensional models e.g. Cauer or Foster-Models. This is not a problem if only one device, which dissipates losses, is considered. But for a thermal observer of an entire power module with multiple paralleled devices this is not accurate anymore, because thermal cross-coupling effects are not included in 1-D models. Furthermore, in future device monitoring systems, it will be essential to monitor the thermal stress at specific locations where it causes damage.

To overcome these limitations, this work demonstrates an enhanced cascaded Luenberger-style 3-D spatial thermal observer for power electronic modules. It is first illustrated how a thermal spatiotemporal state space model of a power module, which has been developed in [13], [14], can be made applicable as a real time model by model truncation. The derivation and implementation of an analytical loss model is then discussed, which can be used to predict losses of each device of a three phase converter dynamically, and also averaged over one fundamental excitation cycle. Based on the loss model and the real time thermal model, a cascaded 3-D observer structure is built, which can dynamically estimate the temperate at the junction and at arbitrary spatial locations within the power module. Then the estimation accuracy (EA) of the observer is evaluated in the presence of model inaccuracies. Finally, the concept is demonstrated experimentally using the Hybridpack2 FS800R07A2E3 (HP2) power module from Infineon, depicted in Fig. 1, whose electro-thermal characterization has been conducted in [13]–[16]. The power module is operated interfaced to a load emulator over realistic mission

978-1-5386-1180-7/18/$31.00 ©2018 IEEE

TABLE I
LATERAL MATERIAL LAYERS OF THE HYBRIDPACK2 POWER MODULE

Material	Depth in µm	k_{th} in $\frac{\mathrm{W}}{\mathrm{m\,K}}$	C_{th} in $\frac{\mathrm{J}}{\mathrm{K}}$	ρ in $\frac{\mathrm{kg}}{\mathrm{m}^3}$
Silicon	67	130	700	2329
Solder Pad	120	57	288	9000
Copper	300	400	385	8700
AlO_2	350	24	880	880
Copper	300	400	385	8700
Solder Layer	300	57	288	9000
Copper	8000	400	385	8700

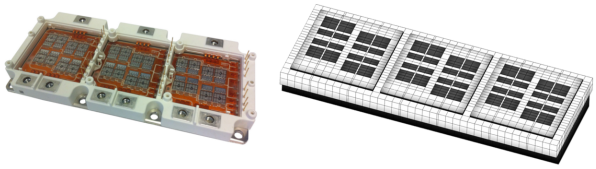

Fig. 1. Hybridpack2 power module and 3-D finite-differnce model structure

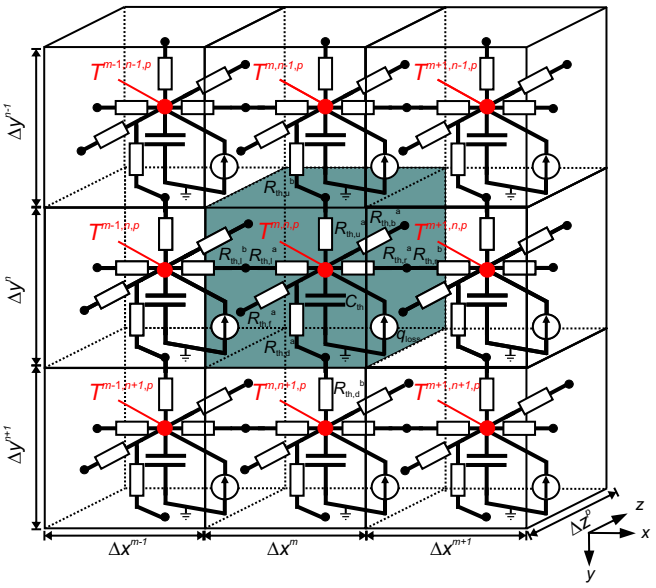

Fig. 2. Thermal network excerpt of the 3-D finite-difference model

profiles to investigate the performance of the observer. In the associated work, presented in [6], the developed observer structure is used for active thermal control of power modules.

II. SPATIAL ELECTRO-THERMAL REAL TIME MODEL

The key component of the spatial thermal observer is the electro-thermal real time model. It consists of a loss model and a compact spatial thermal model, which are reviewed in the following section for one half bridge of the power module.

A. Spatial Thermal Modeling Methodology

For the thermal modeling of the power electronic module, in this example the Hybridpack2 (HP2), the finite difference method (FDM) is used. The thermal modeling methodology has been derived in [13] and [14], and is briefly reviewed in the following. First, the HP2 needs to be structured in small cubes with the spatial coordinates (m,n,p), which is illustrated in Fig. 1. The thermal behavior of each cube can be modeled with a thermal capacitance $C_{\mathrm{th}}^{m,n,p}$ and thermal resistances from each cube to all its neighbors $R_{\mathrm{th,xy}}^{m,n,p}$. A thermal network, which illustrates the heat conduction mechanism of one cube and its neighbor, is depicted in Fig. 2. One linear differential equation can be set up for each cube via (1).

$$C_{\mathrm{th}}^{m,n,p}\frac{\mathrm{d}T^{m,n,p}}{\mathrm{d}t} = -\sum_{i=l}^{b}\frac{T^{m,n,p}}{R_{\mathrm{th,i}}^{m,n,p}} + \frac{T^{m-1,n,p}}{R_{\mathrm{th,l}}^{m,n,p}} + \frac{T^{m+1,n,p}}{R_{\mathrm{th,r}}^{m,n,p}} + \frac{T^{m,n+1,p}}{R_{\mathrm{th,d}}^{m,n,p}} + \frac{T^{m,n-1,p}}{R_{\mathrm{th,u}}^{m,n,p}} + \frac{T^{m,n,p-1}}{R_{\mathrm{th,f}}^{m,n,p}} + \frac{T^{m,n,p+1}}{R_{\mathrm{th,b}}^{m,n,p}} + q_{\mathrm{loss}}^{m,n,p} \tag{1}$$

It predicts the temporal derivative of $T^{m,n,p}$ as a function of the temperatures of all neighbor cubes and the losses $q_{\mathrm{loss}}^{m,n,p}$ generated in all cubes, which represent power devices. The thermal resistances $R_{\mathrm{th,x}}^{m,n,p}$ and thermal capacitances $C_{\mathrm{th}}^{m,n,p}$ can be determined according to (2) and (3).

$$C_{\mathrm{th}}^{m,n,p} = \Delta x^m \Delta y^n \Delta z^p \; c_\rho^{m,n,p} \rho^{m,n,p} \tag{2}$$

$$R_{\mathrm{th,r}}^{m,n,p} = \frac{\Delta x^m}{2 \cdot k_{\mathrm{th}}^{m,n,p} \Delta y^n \Delta z^p} + \frac{\Delta x^{m+1}}{2 \cdot k_{\mathrm{th}}^{m+1,n,p} \Delta y^n \Delta z^p} \tag{3}$$

They can be calculated as a function of the geometrical dimensions of the cube and its neighbors, and based on the material properties summarized in Tab. I. Note, that in (3) the resistance between one cube and its neighbor to the right (in x- axis direction) is given as an example.

The thermal interface between the pin fin heat sink of the power module and the cooling liquid can be modeled with an effective convection resistance R_{conv} for each cube interfacing the cooling fluid. The convective heat transfer resistance can be determined via (4) based on the surface area of the cubes $A = \Delta x^m \Delta z^p$ and the heat transfer coefficient of the heat sink. It was determined in [14] for ethylene-glycol water at a flow rate of 10 L/ min and a temperature of 20 °C to $h_{\mathrm{eff}} = 3\ \mathrm{W/(Kcm^2)}$.

$$R_{\mathrm{conv}}^{\mathrm{m,p}} = \frac{1}{h_{\mathrm{eff}} \cdot \Delta x^m \Delta z^p} \tag{4}$$

B. Setup of a Spatial Thermal State Space Model

The differential equations of all cubes can be represented in one linear state space model according to (5).

$$\frac{\mathrm{d}\underline{\boldsymbol{T}}}{\mathrm{d}t} = \boldsymbol{A} \cdot \underline{\boldsymbol{T}} + \boldsymbol{B} \cdot \underline{\boldsymbol{P}}_{\mathbf{loss}} \qquad \underline{\boldsymbol{T}}_{\mathrm{out}} = \boldsymbol{C} \cdot \underline{\boldsymbol{T}} \tag{5}$$

The temperature vector $\underline{\boldsymbol{T}}$ represents the temperatures $T^{m,n,p}$ of all nodes throughout the power module, whereas the loss vector $\underline{\boldsymbol{P}}_{\mathrm{loss}}$, given by equation (6), represents the losses of all IGBTs and diodes within one half bridge.

$$\underline{\boldsymbol{P}}_{\mathrm{loss}} = \left(P_{\mathrm{loss}}^{\mathrm{IGBTA}} \;\; P_{\mathrm{loss}}^{\mathrm{DiodeA}} \;\; P_{\mathrm{loss}}^{\mathrm{IGBTB}} \;\; P_{\mathrm{loss}}^{\mathrm{DidoeB}}\right)^{\mathrm{T}}. \tag{6}$$

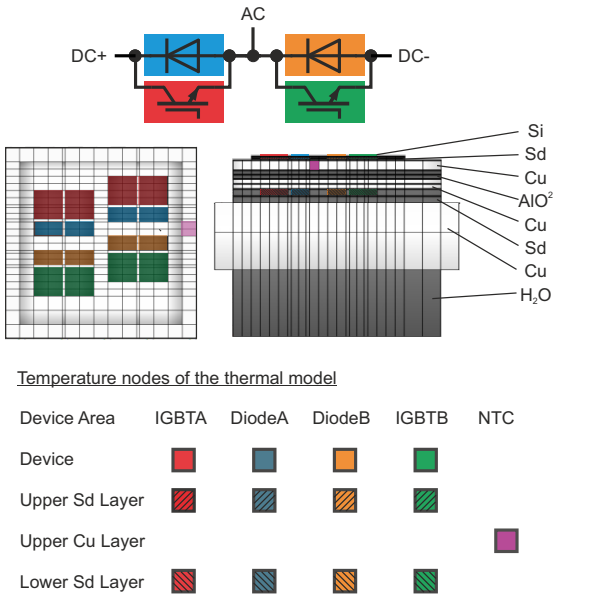

Fig. 3. Visualization of the spatial temperature nodes of interest for temperature monitoring of one Hybridack2 half bridge

All thermal resistances and capacitances of the finite difference model are reflected in the input matrix $\boldsymbol{B}$ and the transition matrix $\boldsymbol{A}$. The output equation (7) allows the specification of temperature nodes or the average temperature over a defined volume, that should be provided at the output of the observer structure for thermal monitoring or control. This is realized with the output matrix $\boldsymbol{C}$.

$$\underline{\boldsymbol{T}}_{\mathrm{out}} = \boldsymbol{C} \cdot \underline{\boldsymbol{T}} \tag{7}$$

The volume elements whose average temperature is selected for the output vector $\underline{\boldsymbol{T}}_{\mathrm{out}}$ are illustrated in Fig. 3. These include the average device temperatures $\underline{\boldsymbol{T}}_{\mathrm{j}}$, the temperature of the solder interconnect below each device $\underline{\boldsymbol{T}}_{\mathrm{sd,up}}$, the interconnect temperature between the DCB and the base plate $\underline{\boldsymbol{T}}_{\mathrm{sd,down}}$ below each device, and the module temperature at the location of the thermistor T_{NTC}. Thus, the output vector $\underline{\boldsymbol{T}}_{\mathrm{out}}$ is given according to (8).

$$\underline{\boldsymbol{T}}_{\mathrm{out}} = \left(\underline{\boldsymbol{T}}_{\mathrm{j}} \;\; \underline{\boldsymbol{T}}_{\mathrm{sd,up}} \;\; \underline{\boldsymbol{T}}_{\mathrm{sd,down}} \;\; T_{\mathrm{NTC}}\right)^{\mathrm{T}} \tag{8}$$

Note, that each component of (8) is itself a vector with four components structured according to (9), as every critical component of the power module is evaluated below all four devices of a half bridge.

$$\underline{\boldsymbol{T}}^{\mathrm{x}} = \left(T_{\mathrm{x}}^{\mathrm{IGBTA}} \;\; T_{\mathrm{x}}^{\mathrm{DiodeA}} \;\; T_{\mathrm{x}}^{\mathrm{IGBTB}} \;\; T_{\mathrm{x}}^{\mathrm{DidoeB}}\right)^{\mathrm{T}} \tag{9}$$

All matrices of the state space model have been derived with the MATLAB based software framework for thermal modeling of power modules, which is illustrated in [13], [14]. The resulting spatial state space model estimates the temperature of the power module at critical design elements which suffer from degradation. In the next sections, it is demonstrated how this model can be implemented as a real time model on a DSP system.

C. Thermal Model Reduction and Discretization

Unfortunately, the developed state space model exhibits far too many states, such that it is not suitable for real time applications. However, model reduction techniques are a very powerful tool to reduce the order of large scale physical system models with potentially small loss of model accuracy.

1) Balanced Truncation: For the reduction of the large scale thermal model of the power module the balanced truncation method [17] is used in this work. In principle, the balanced truncation uses a base transformation (10), which sorts the states according to their energy transfer between the system inputs and outputs.

$$\underline{\boldsymbol{\theta}} = \boldsymbol{M} \cdot \underline{\boldsymbol{T}} \qquad \underline{\boldsymbol{T}} = \boldsymbol{M}^{-1} \cdot \underline{\boldsymbol{\theta}} \tag{10}$$

The system matrices are transformed according to (11).

$$\tilde{A} = \boldsymbol{M}\boldsymbol{A}\boldsymbol{M}^{-1} \qquad \tilde{\boldsymbol{B}} = \boldsymbol{M}\boldsymbol{B} \qquad \tilde{\boldsymbol{C}} = \boldsymbol{C}\boldsymbol{M}^{-1}. \tag{11}$$

Note that the physical meaning of the states, which originally reflect the temperature at various nodes of the thermal model, gets lost. Nevertheless, this transformation does neither change dynamics, i. e. the eigenvalues of the system, nor the input-output behavior of the system.

After the base transform $\boldsymbol{M}$ ordered the n states according to their importance for the energy transfers between system inputs and outputs, the system can be split in two parts, which are illustrated in (12).

$$\frac{\mathrm{d}}{\mathrm{d}t}\begin{pmatrix}\underline{\boldsymbol{\theta}}_1\\ \underline{\boldsymbol{\theta}}_2\end{pmatrix} = \begin{pmatrix}\tilde{\boldsymbol{A}}_{11} & \tilde{\boldsymbol{A}}_{12}\\ \tilde{\boldsymbol{A}}_{21} & \tilde{\boldsymbol{A}}_{22}\end{pmatrix}\begin{pmatrix}\underline{\boldsymbol{\theta}}_1\\ \underline{\boldsymbol{\theta}}_2\end{pmatrix} + \begin{pmatrix}\tilde{\boldsymbol{B}}_1\\ \tilde{\boldsymbol{B}}_2\end{pmatrix}\underline{\boldsymbol{P}}_{\mathrm{loss}} \tag{12}$$

The first part of the system, including the first r states, is handling most of the energy transfers between input and outputs, whereas the remaining $n-r$ states are only capturing a negligible amount of energy transfers. As a consequence, the system can be truncated by only taking into account the most important states for energy transfer and leaving out all others. This leads to a truncated system according to (13).

$$\frac{\mathrm{d}\underline{\boldsymbol{\theta}}_1}{\mathrm{d}t} = \tilde{\boldsymbol{A}}_{11}\underline{\boldsymbol{\theta}}^1 + \tilde{\boldsymbol{B}}_1\underline{\boldsymbol{P}}_{\mathrm{loss}} \qquad \underline{\boldsymbol{T}}_{\mathrm{out}} = \boldsymbol{C} \cdot \boldsymbol{M}^{-1}\underline{\boldsymbol{\theta}}_1 \tag{13}$$

2) Analysis of the Truncation Error: A time domain evaluation of the truncation error of the thermal impedance, conducted in [14], indicates that a truncated model with 14 states should provide a reasonable precision. Fortunately, this is also a reasonable model size, such that an implementation on a standard DSP with a sampling frequency in the range of 1 kHz is feasible. For a more in depth analysis of the truncation error the estimation accuracy (EA) given by (14) is a suitable metric.

$$\mathrm{EA}(j\omega) = \frac{\hat{T}_{\mathrm{x}}(\mathrm{j}\omega)}{T_{\mathrm{x}}(\mathrm{j}\omega)} = \frac{\hat{T}_{\mathrm{x}}(\mathrm{j}\omega)}{P_{\mathrm{loss}}^{\mathrm{IGBT}}(\mathrm{j}\omega)} \cdot \left(\frac{T_{\mathrm{x}}(\mathrm{j}\omega)}{P_{\mathrm{loss}}^{\mathrm{IGBT}}(\mathrm{j}\omega)}\right)^{-1} \tag{14}$$

The estimation accuracy is determined and plotted in Fig. 4 above the frequency response function $T_{\mathrm{x}}(j\omega)/P_{\mathrm{loss}}^{\mathrm{IGBT}}(j\omega)$ for specific spatial nodes of the power module assuming heat injection via IGBT A only. The evaluated temperature nodes

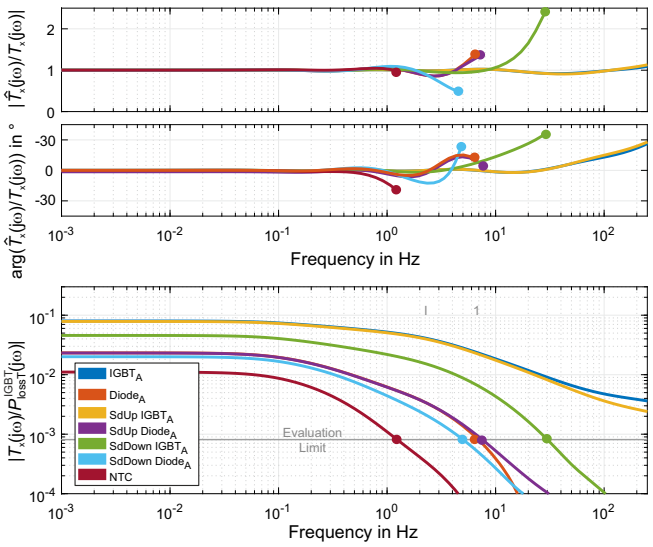

Fig. 4. Estimation accuracy of the truncatd thermal model with 14 states evaluated at the IGBT A, Diode A, upper and lower solder (Sd) layer at both devices and NTC indicated in Fig. 3 (top).
Frequency response plot of the identical temperatures nodes for loss injection at IGBT A (bottom)

are visualized in Fig. 3. At the frequency range where the frequency response function reaches $1/1000\ \mathrm{K/W}$ the EA plot is stopped. This is because at higher frequencies even a loss excitation of 1000 W results in a temperature amplitude of less than 1 K, which can be neglected. The resulting EA plot reveals that the truncated model with 14 states is able to predict the thermal behavior of the power module with very good accuracy in amplitude and phase at the selected spatial nodes over the frequency range of interest. Note that the accuracy of the truncated model at higher frequencies can be improved by a higher model rank r.

3) Implementation of the truncation process: The MATLAB Control systems toolbox exhibits a balanced truncation algorithm *balred*, which is used for this work. It requires a computation time of approximately two hours ones to compute the balanced realization of the original thermal model with 9142 states. The system can be directly truncated to any desired order, afterwards. A more detailed discussion on the balanced truncation of thermal models can be found in [14].

4) Discretization: In a last step the thermal model (13) is discretized using the zero-order hold method [18]. The discrete time model has the format of a matrix difference equations (15), that can simply compute the temperature vector $\underline{\boldsymbol{\theta}}_1(k+1)$ one time step T_s ahead.

$$\underline{\boldsymbol{\theta}}_1(k+1) = \tilde{\boldsymbol{A}}^\mathrm{d} \cdot \underline{\boldsymbol{\theta}}_1(k) + \tilde{\boldsymbol{B}}^\mathrm{d} \cdot \underline{\boldsymbol{P}}^\mathrm{d}_\mathbf{loss}(k). \tag{15}$$

This allows accurate thermal modeling in discrete time, if the losses do not significantly change over one computation interval T_s. A computation interval of $Ts = 1\,\mathrm{ms}$ is used in this work to ensure that the system dynamics are accurately discretized for excitations up to 100 Hz. If the thermal model should accurately estimate the system response at higher excitation frequencies, the truncation rank r must be increased

TABLE II
CONDUCTION LOSS PARAMETERS OF THE HP2 POWER MODULE

T_j	V_ce	R_ce	S_ce	V_T	R_T	S_T
25 °C	542 mV	0 Ω	0.03 V/A$^{0.5}$	334 mV	0 Ω	0.064 V/A$^{0.5}$
125 °C	307 mV	0.2 mΩ	0.041 V/A$^{0.5}$	222 mV	0 Ω	0.060 V/A$^{0.5}$

and the sampling interval T_s must be decreased.

The discrete time matrices $\boldsymbol{A}^\mathrm{d}$ and $\boldsymbol{B}^\mathrm{d}$ are calculated according to (16), which is a computation also supported by the *c2d* algorithm of the MATLAB Control System Toolbox.

$$\tilde{\boldsymbol{A}}^\mathrm{d} = \mathrm{e}^{\tilde{\boldsymbol{A}}_{11}\cdot T_\mathrm{s}} \text{ and } \tilde{\boldsymbol{B}}^\mathrm{d} = \int_{t=0}^{T_\mathrm{s}} \tilde{\boldsymbol{B}}_1 \mathrm{e}^{\tilde{\boldsymbol{A}}_{11}\cdot\tau}\mathrm{d}\tau \tag{16}$$

The output matrix $\boldsymbol{C}$ remains unaffected by the discretization such that the output equation is given according to (17).

$$\underline{\boldsymbol{T}}_\mathrm{out} = \tilde{\boldsymbol{C}}^\mathrm{d}\underline{\boldsymbol{\theta}}_1 \quad \text{with} \quad \tilde{\boldsymbol{C}}^\mathrm{d} = \boldsymbol{C}\cdot\boldsymbol{M}^{-1} \tag{17}$$

The resulting truncated and discretized spatiotemporal thermal state space model is used for the implementation of the observer structure.

D. IGBT and Diode Loss Modeling

In the following, models for the prediction of dynamic and averaged losses are presented based on the work in [14]. The dynamic loss model is used to predict the instantaneous losses of the devices, which occur over one PWM switching cycle of the converter. The average loss model, is developed based on the dynamic loss model, and determines the average losses, that are dissipated in the devices over one period of the excitation frequency. Its loss estimates do not exhibit cycles due to the sinusoidal current variations at the excitation frequency.

1) Dynamic loss model: First the conduction losses of the IGBT and the diode within one half bridge are addressed. They are dependent on the duty cycle $d_\mathrm{conv,A}$, the device current i_ce and i_d as well as on the forward voltage of the IGBT $v_\mathrm{ce}^\mathrm{IGBT}$ and the diode $v_\mathrm{T}^\mathrm{Diode}$. Conduction losses can be determined based on (18).

$$\begin{aligned} P_\mathrm{cond}^\mathrm{IGBT} &= v_\mathrm{ce}^\mathrm{IGBT}(i_\mathrm{ce},T)\cdot i_\mathrm{ce}\cdot d_\mathrm{conv,A} \\ P_\mathrm{cond}^\mathrm{Diode} &= v_\mathrm{T}^\mathrm{Diode}(i_\mathrm{d},T)\cdot i_\mathrm{d}\cdot(1-d_\mathrm{conv,A}) \end{aligned} \tag{18}$$

The forward voltages $v_\mathrm{ce}^\mathrm{IGBT}$ and $v_\mathrm{T}^\mathrm{Diode}$ have been modeled based on extracted data sheet parameters, summarized in Tab. II, and are approximated as a function of the temperature T and the current i_ce according to (19).

$$\begin{aligned} v_\mathrm{ce}^\mathrm{IGBT}(i_\mathrm{ce},T) &= V_\mathrm{ce}(T) + R_\mathrm{ce}(T)i_\mathrm{ce} + S_\mathrm{ce}(T)\sqrt{i_\mathrm{ce}} \\ v_\mathrm{T}^\mathrm{Diode}(i_\mathrm{d},T) &= V_\mathrm{T}(T) + R_\mathrm{T}(T)i_\mathrm{d} + S_\mathrm{T}(T)\sqrt{i_\mathrm{d}} \end{aligned} \tag{19}$$

The conduction loss parameters at a particular temperature are determined by interpolation of the parameters in Tab. II.

Next, step the switching loss model is addressed. It is based on more than 700 double pulse measurements, which have been conducted with the Hybridpack2 power module on a temperature controlled double pulse test bench [19], [20]. Based on the measured switching energies of the IGBTs and

TABLE III
SWITCHING LOSS PARAMETERS OF THE HP2 POWER MODULE FOR THE REFERENCE POINT $V_{\mathrm{dc}}^{\mathrm{ref}} = 400$ V, $R_{\mathrm{g}}^{\mathrm{ref}} = 2.2\ \Omega$ AND $T^{\mathrm{ref}} = 20$ °C

E_0	K_0	α	β	K_{T}	E_0^{rr}	K_0^{rec}	$K_{\mathrm{T}}^{\mathrm{rec}}$
1.2 mJ	0.1 mJ/ A	1.75	0.82	1 µJ/ K	0.5 mJ	4.4 µJ/ A	0.02 1/ K

the diodes, the following empirical model has been derived in [14]. It determines the losses based on the device current of the IGBT and diode i_{ce} and i_{d}, the dc-link voltage V_{dc}, the gate resistance R_{g} and the device temperature T_{j}.

$$E_{\mathrm{sw}}^{\mathrm{IGBT}} = E_0 + K_0 i_{\mathrm{ce}} \left(\frac{V_{\mathrm{dc}}}{V_{\mathrm{dc}}^{\mathrm{ref}}}\right)^{\alpha} \cdot \left(\frac{R_{\mathrm{g}}}{R_{\mathrm{g}}^{\mathrm{ref}}}\right)^{\beta} + \Delta T_{\mathrm{j}} \cdot K_{\mathrm{T}} \tag{20}$$

$$E_{\mathrm{sw}}^{\mathrm{D}} = \left(E_0^{\mathrm{rec}} + K_0^{\mathrm{rec}} i_{\mathrm{ce}} \left(\frac{V_{\mathrm{dc}}}{V_{\mathrm{dc}}^{\mathrm{ref}}}\right)^{\alpha} \left(\frac{R_{\mathrm{g}}}{R_{\mathrm{g}}^{\mathrm{ref}}}\right)^{-\beta}\right) \cdot (1 + \Delta T_{\mathrm{j}} \cdot K_{\mathrm{T}}^{\mathrm{rec}})$$

$$\text{with } \Delta T_{\mathrm{j}} = T_j - T_{\mathrm{j}}^{\mathrm{ref}} \text{ and } E_0^{\mathrm{rec}} = E_0^{\mathrm{rr}} \cdot \frac{V_{\mathrm{dc}}}{V_{\mathrm{dc}}^{\mathrm{ref}}} \tag{21}$$

The switching energies of the IGBT and diode $E_{\mathrm{sw}}^{\mathrm{IGBT}}$ and $E_{\mathrm{sw}}^{\mathrm{D}}$ can be directly related to the switching losses via (22).

$$P_{\mathrm{sw}}^{\mathrm{IGBT}} = E_{\mathrm{sw}}^{\mathrm{IGBT}} \cdot f_{\mathrm{sw}} \quad \text{and} \quad P_{\mathrm{sw}}^{\mathrm{D}} = E_{\mathrm{sw}}^{\mathrm{D}} \cdot f_{\mathrm{sw}} \tag{22}$$

2) Averaged loss model: Based on the transient loss model, an averaged loss model is built that predicts the average losses, which occur over one electrical period $T_0 = 2\pi/\omega_0$. Due to the symmetrical operation the losses for both IGBTs within one half bridge are identical. The same holds for both diodes. The load current of the devices is given according to (23). The current ripple is neglected in this expression, as it only has a minor impact on the conduction losses losses [21].

$$i_{\mathrm{ce}}(t) = \begin{cases} \hat{I} \cdot \sin(\omega_0 t) & \text{if } \omega_0 t < \pi + 2\pi \cdot n \\ 0 & \text{if } \omega_0 t > \pi + 2\pi \cdot n \end{cases} \tag{23}$$

The duty cycle of the half bridge d, which indicates the conduction interval of the upper device, depends significantly on the used modulation scheme. In case of a standard sine-triangular modulation, which is discussed in this work, it exhibits a constant and a sinusoidal component and is given according to (24).

$$d(t) = \frac{1}{2} \cdot (1 + M \sin(\omega_0 \cdot t + \varphi_0)) \quad \text{with} \quad M = \frac{\hat{V}}{V_{\mathrm{dc}}} \tag{24}$$

It is a function of the modulation index M, which is the ratio between voltage amplitude $\hat{V}$ and the dc-link voltage U_{dc}, the fundamental frequency ω_0 and the phase angle φ_0 between voltage $\hat{V}$ and current $\hat{I}$. Based on the device current i_{ce} and the duty cycle d , the average conduction losses of the IGBT can be determined via (25).

$$\bar{p}_{\mathrm{cond}}^{\mathrm{IGBT}} = \frac{1}{T_0} \int_{t=0}^{T_0} i_{\mathrm{ce}} \cdot v_{\mathrm{ce}}(i_{\mathrm{ce}}, T_{\mathrm{j}}) \mathrm{d}t \tag{25}$$

By inserting (19) into (25) the averaged losses (26) are derived:

$$\bar{p}_{\mathrm{cond}}^{\mathrm{IGBT}} = V_{\mathrm{ce}} \hat{I} \cdot \left(\frac{1}{2\pi} + \frac{M \cos(\varphi_0)}{8}\right) + R_{\mathrm{ce}} \hat{I}^2 \cdot \left(\frac{1}{8} + \frac{M \cos(\varphi_0)}{3\pi}\right) + S_{\mathrm{ce}} \cdot \hat{I}^{\frac{3}{2}} \cdot (0.139 + 0.1144 \cdot M \cos(\varphi_0)) \tag{26}$$

Similarly, with the complimentary duty cycle $\bar{d} = 1 - d$, the conduction losses of the diode can be calculated via (27).

$$\bar{p}_{\mathrm{cond}}^{\mathrm{Diode}} = V_{\mathrm{T}} \hat{I} \cdot \left(\frac{1}{2\pi} - \frac{M \cos(\varphi_0)}{8}\right) + R_{\mathrm{T}} \hat{I} \cdot \left(\frac{1}{8} - \frac{M \cos(\varphi_0)}{3\pi}\right) + S_{\mathrm{T}} \cdot \hat{I} \cdot (0.139 - 0.1144 \cdot M \cdot \cos(\varphi_0)) \tag{27}$$

The averaged switching losses can be derived analogously via (28). It should be pointed out that the switching losses do not depend on the modulation index M or the phase angle φ_0, but only depend on the current amplitude $\hat{I}$.

$$\bar{p}_{\mathrm{sw}}^{\mathrm{IGBT}} = \int_{t_0}^{t_0+T_0} p_{\mathrm{sw}}^{\mathrm{IGBT}}(i_{\mathrm{ce}}, T_{\mathrm{j}}, U_{\mathrm{dc}}, R_{\mathrm{g}})\ \mathrm{d}t = \left(\frac{E_0}{2} + \frac{K_0}{\pi} \hat{I} \left(\frac{U_{\mathrm{dc}}}{U_{\mathrm{dc}}^{\mathrm{ß}}}\right)^{\alpha} \left(\frac{R_{\mathrm{g}}}{R_{\mathrm{g}}}\right)^{\beta} + \Delta T_{\mathrm{j}} \frac{K_{\mathrm{T}}}{2}\right) \cdot f_{\mathrm{pwm}} \tag{28}$$

Finally, the averaged switching losses of the diode can be predicted based on (29).

$$\bar{p}_{\mathrm{sw}}^{\mathrm{Diode}} = \left(\frac{E_0^{\mathrm{rec}}(U_{\mathrm{dc}})}{2} + \frac{K_0{}^{\mathrm{rec}}}{\pi} \cdot \hat{I} \cdot \left(\frac{U_{\mathrm{dc}}}{U_{\mathrm{dc}}^{\mathrm{ref}}}\right)^{\alpha} \cdot \left(\frac{R_{\mathrm{g}}}{R_{\mathrm{g}}^{\mathrm{ref}}}\right)^{-\beta}\right) \cdot \left(1 + \left(T_{\mathrm{j}} - T_{\mathrm{j}}^{\mathrm{ref}}\right) \cdot K_{\mathrm{T}}^{\mathrm{rec}}\right) \cdot f_{\mathrm{pwm}} \tag{29}$$

It must be emphasized, that the averaged switching loss model can be generally applied for operation with sinusoidal load currents, whereas the conduction loss model only holds for sine-triangular modulation. For any other modulation technique, e.g. space vector modulation the integral (25) must be solved again for the corrected duty cylcle, which results from the particular modulation method.

III. CASCADED THERMAL OBSERVER

An enhanced cascaded Luenberger-style spatial thermal observer structure has been developed based on the derived electro-thermal model. Its state block diagram is depicted in Fig. 5. The model based temperature estimation process is corrected in the observer by device temperature measurements $\underline{\boldsymbol{T}}_{\mathrm{j}}$, which are realized with IR-sensors in this work. These exhibit a delay of 10 ms and add noise to the measurement signals, which must be considered for the observer design. In a later application they will be replaced by less invasive junction temperature estimation techniques e.g. on-chip temperature sensor [22], collector-emitter voltage sensing [12] gate voltage plateau sensing [23] or gate current sensing [24].

The observer structure exhibits two stages. The first stage estimates the instantaneous temperature within the power module for monitoring and fault detection. The instantaneous temperature exhibits slow cycles, due to load variations, and fast cycles, due excitation by the sinusoidal current. The second observer stage estimates the averaged temperature of the power module. It aims to eliminate the thermal cycles at the excitation frequency. The resulting averaged temperature is estimated with nearly zero lag, such that it can be effectively used for active thermal control algorithms e.g. in [6].

Within the first observer stage the thermal real time model predicts the transient temperature vector $\underline{\hat{\boldsymbol{T}}}_{\mathrm{out}}$, which has been

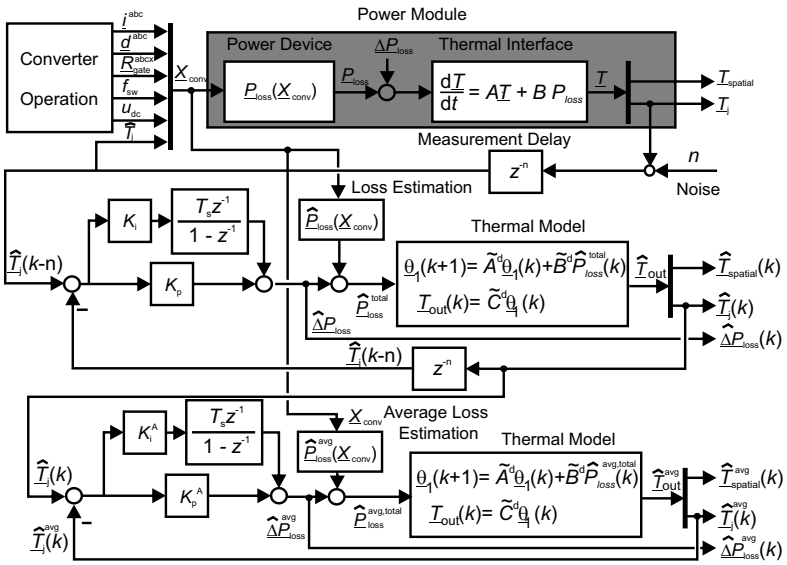

Fig. 5. State block diagram of the enhanced cascaded Luenberger-Style spatial thermal observer structure

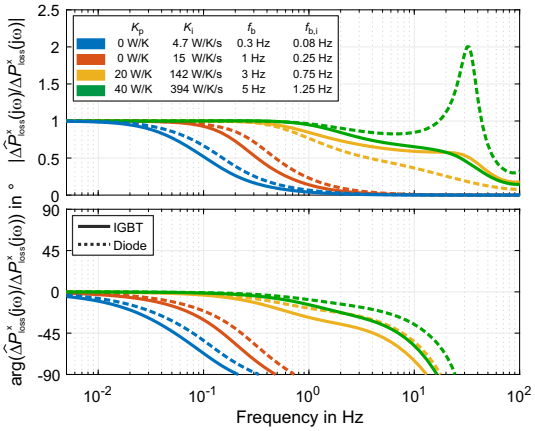

Fig. 6. Loss error estimation accuracy of the closed loop observer at different bandwidths

defined in equation (8), based on the loss estimates $\hat{\underline{P}}_{\mathrm{loss}}$, which are provided by the observer feedforward path. The obtained junction temperature estimates of the four devices $\hat{\underline{T}}_{\mathrm{j}}$ are compared with junction temperature measurements $\underline{T}_{\mathrm{j}}$. If the junction temperature measurements are delayed by n samples of T_{s} due to the sensor, this delay must be also applied to the estimates before the comparison to ensure consistency. The junction temperature estimation error of each device $\Delta\hat{\underline{T}}_{\mathrm{j}}$ is passed to a proportional-integral (PI) regulator. It corrects the loss prediction of the open loop model $\hat{\underline{P}}_{\mathrm{loss}}$ by the loss error estimate $\Delta\hat{\underline{P}}_{\mathrm{loss}}$, if the junction temperature prediction and measurement deviate from each other. Thereby, deviations between the model and the physical system are directly detected and compensated.

This correction makes the observer resilient against modeling errors, that can result from parameter deviations of the loss model or inaccuracies of the thermal model. In addition, the loss error estimate $\Delta\hat{\underline{P}}_{\mathrm{loss}}$ can exhibit valuable information about potential degradation or malfunction of the power module. If its average value rises rapidly, after long term operation of the power module, this indicates that more losses are generated, for example due to partial device failures as a consequence of bond wire lift-offs [12]. A slow rise of this signal might indicate that the thermal interface, provided by the power module, is degraded, e.g. due to delamination within the power module as illustrated in [7], [12]. In both cases $\Delta\hat{\underline{P}}_{\mathrm{loss}}$ is a valuable monitoring signal to detect possible module failures before they occur.

The second cascaded observer stage is fed with the device loss estimates, averaged over one electrical excitation period $\hat{\underline{P}}_{\mathrm{loss}}^{\mathrm{avg}}$, in order to predict averaged temperature estimates $\hat{\underline{T}}_{\mathrm{out}}^{\mathrm{avg}}$. The averaged junction temperature estimates $\underline{T}_{\mathrm{j}}^{\mathrm{avg}}$ are compared with the transient junction temperature estimates $\hat{\underline{T}}_{\mathrm{j}}$, which are contained in the output of the first observer stage. The error is fed to the PI regulator of the second observer stage to compensate for errors of the models. The regulator gains of the second stage are selected small enough, such that they only compensate deviations slowly, and do not introduce thermal cycles at the fundamental electrical frequency.

A final aspect, to be considered for the averaged temperature estimation, is the behavior of the averaged loss model at low excitation frequencies. At low excitation frequencies the averaged loss model does not reflect the actual losses anymore, because the losses are concentrated on specific devices, dependent on the current direction. To avoid this, the averaged loss model is replaced by the transient loss model at excitation frequencies bellow 0.5 Hz

IV. Design and Analysis

In the following, the design of both observer stages is discussed. The performance of the observer structure is analyzed by estimation accuracy evaluation of the temperature estimates and the loss error.

A. Transient Temperature Estimation

The design of the feedback gains K_{p} and K_{i} is critical for the effective combination of model based temperature prediction and the sensor based temperature correction. They determine the bandwidth, in which the sensors can correct prediction error caused by inaccuracies of the models.

For a simple and meaningful derivation of observer feedback gains, the thermal capacitance C_{th} and the the thermal resistance R_{th} of a first order thermal model of the IGBT and the diode are derived. Firstly, the thermal impedance model is extracted for the IGBT and the diode from the spatial state space model (5). The thermal impedance model is then reduced to a first-order model by balanced truncation, and the resulting eigenvalue and gain are identified. They can be directly related to a thermal resistance R_{th} and a thermal

capacitance C_{th} of the IGBT and the diode. In this work, the feedback gains of the observer shall be kept identical for all devices. Therefore, the thermal capacitance and thermal resistance of the diode and the IGBT are averaged resulting into $C_{\mathrm{th}} = 1.6\ \mathrm{J/K}$ and $R_{\mathrm{th}} = 0.1\ \mathrm{K/W}$.

The observer feedback gains are designed for one device independently from the other, because the resulting approximation error is tolerable. The closed loop eigenvalues of the feedback loop created by the first order thermal impedance model, characterized by R_{th} and C_{th}, and the PI regulator of the observer with the gains K_{p} and K_{i}, are given according to (30).

$$s_{1,2} = -\frac{R_{\mathrm{th}}^{-1} + K_{\mathrm{p}}}{2C_{\mathrm{th}}} \pm \sqrt{\left(\frac{R_{\mathrm{th}}^{-1} + K_{\mathrm{p}}}{2C_{\mathrm{th}}}\right)^2 - \frac{K_{\mathrm{i}}}{C_{\mathrm{th}}}} \tag{30}$$

They can be approximated according to (31), if the system is over-critically damped and the eigenvalues are placed on the real axis.

$$s_1 \approx \frac{K_{\mathrm{p}} + R_{\mathrm{th}}^{-1}}{C_{\mathrm{th}}} \text{ and } s_2 = -\frac{K_{\mathrm{i}}}{K_{\mathrm{p}} + R_{\mathrm{th}}^{-1}} \tag{31}$$

The placement of an eigenvalue on the real axis can be directly related to a associated time constant τ and bandwidth ω_{b} according to $s_{\mathrm{EV}} = -1/\tau_{\mathrm{EV}} = -\omega_{\mathrm{b}}$. As a consequence, the observer feedback gains K_{p} and K_{i} can be determined via (32) by specification of the bandwidth $f_{\mathrm{b,p}}$ and $f_{\mathrm{b,i}}$ of the proportional and the integral integral feedback path.

$$K_{\mathrm{p}} = 2\pi f_{\mathrm{b,p}} C_{\mathrm{th}} - R_{\mathrm{th}}^{-1} \qquad K_{\mathrm{i}} = 2\pi f_{\mathrm{b,i}} \left(K_{\mathrm{p}} + R_{\mathrm{th}}^{-1}\right) \tag{32}$$

The integral feedback gain of the observer K_{i} determines the bandwidth $f_{\mathrm{b,i}}$, in which the integral feedback path dominates the correction process of the temperature estimates. In this frequency range zero steady-state error can be achieved. The proportional feedback gain K_{p} selects the bandwidth $f_{\mathrm{b,p}}$, in which the proportional feedback path dominates the correction process of the temperature estimates. Above the proportional feedback bandwidth $f_{\mathrm{b,p}}$ the temperature estimate depends only on the quality of the loss model and the thermal model. It is not corrected anymore by the temperature measurements. In this work, the bandwidth of the integral state feedback loop $f_{\mathrm{b,i}}$ is kept a factor of four below the bandwidth of the proportional feedback loop $f_{\mathrm{b,p}}$. This ensures that the closed loop EVs remain over-critically damped, are located on the real axis and can be approximated by (31).

In the following, the effect of different bandwidths f_{b} is discussed based on the loss error estimation accuracy plot in Fig. 6. The loss error estimation accuracy provides a metric in the frequency domain, that tells how well the observer estimates losses $\Delta\underline{\boldsymbol{P}}_{\mathrm{loss}}$, which occur in the converter but are not taken into account by the loss model. The loss error estimation accuracy in Fig. 6 shows that, within the integral bandwidth of the observer, the loss error is estimated without steady-state error. Within the proportional bandwidth the loss error is estimated with a steady-state error that can be reduced with higher proportional feedback gains K_{p}. Above the the

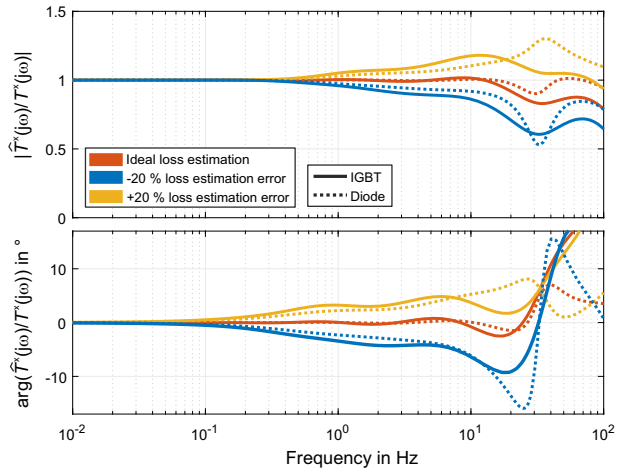

Fig. 7. Estimation accuracy of the transient junction temperature with and without error in the loss estimation

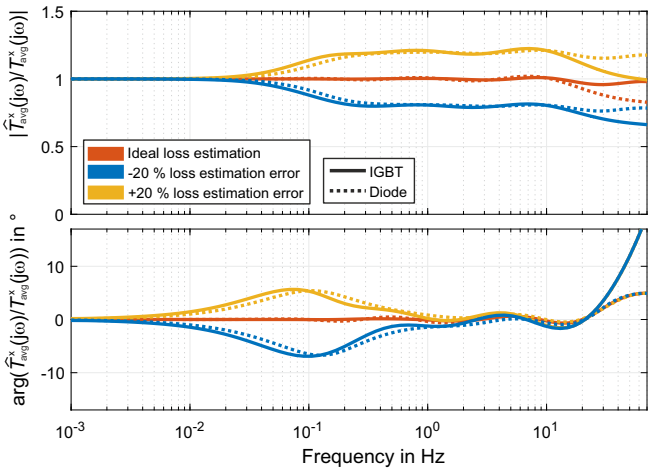

Fig. 8. Estimation accuracy of the averaged junction temperature with and without error in the loss estimation

proportional bandwidth the loss error cannot be estimated anymore. The selection of higher feedback gains increases the bandwidth of the loss error estimation. Due to the delays in the feedback loop, the maximum bandwidth is limited. If the bandwidth approaches this limit, the excitation of resonances become visible and degrade the performance of the estimation process.

For the power module and sensors, which are used in this work, the feedback gains and bandwidths have been summarized in Tab. IV. They were used to determine the closed loop estimation accuracy (EA) of the diode and the IGBT junction temperature, that has been plotted in Fig. 7. The EA plots demonstrate that the observer, which uses the truncated thermal model with 14 states, can estimate the junction temperatures of the devices over a wide frequency range. The magnitude error of the estimates is bounded by the error of the loss estimation. Even more important, the phase of the estimates exhibits nearly zero phase lag for all EA plots. Small additional phase and magnitude errors are induced above

TABLE IV
THERMAL MODEL PARAMETERS AND FEEDBACK GAINS FOR THE HP2

Model	C_{th}	$f_{\mathrm{b,p}}$	$f_{\mathrm{b,i}}$	K_{p}	K_{i}
Transient	1.6 J/K	4 Hz	0.8 Hz	30 W/K	200 W/K/s
Averaged	1.6 J/K	1 Hz	0.3 Hz	-	18 W/K/s

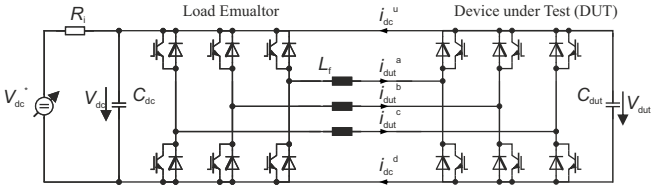

Fig. 9. Topology of the load emulator test bench

20 Hz. These result from the limited high frequency accuracy of the truncated loss model with 14 states and can be omitted using a thermal model with more states The evaluation of the truncated thermal model in Fig. 4 suggests, that the same performance can be achieved for the estimation of spatial temperature information.

B. Averaged Temperature Estimation

The second stage of the observer estimates averaged spatial temperatures $\hat{\underline{T}}_{\mathrm{out}}^{\mathrm{avg}}$ with nearly zero lag. This feature is very important for active thermal control e.g. as presented in [6]. The feedback gains of the second observer stage, $K_{\mathrm{p}}^{\mathrm{A}}$ and $K_{\mathrm{i}}^{\mathrm{A}}$, are used to set the bandwidth, in which the prediction of averaged temperature can be corrected by the estimates of the first observer stage. It is important to keep the bandwidth of the second observer stage low enough, such that the fundamental thermal cycles are not induced in the averaged temperature estimate. For this reason, the integral bandwidth of the second observer stage has been set to $f_{\mathrm{b,i}} = 0.3$ Hz in this work using (32). Note, that the proportional bandwidth of the observer is primarily provided the thermal resistance R_{th}^{-1}, such that any feedback gain $K_{\mathrm{p}}^{\mathrm{A}}$ does not make a significant difference.

The performance of the averaged temperature estimation can be examined based on the estimation accuracy plot in Fig. 8. It demonstrates that the averaged device temperatures are estimated over a wide temperature range with nearly zero lag. even in case of loss estimation errors.

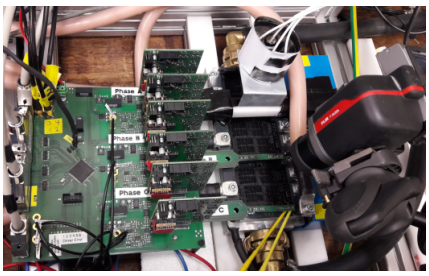

Fig. 10. Hybridpack2 power module equipped with IR sensors on the load emulator test bench

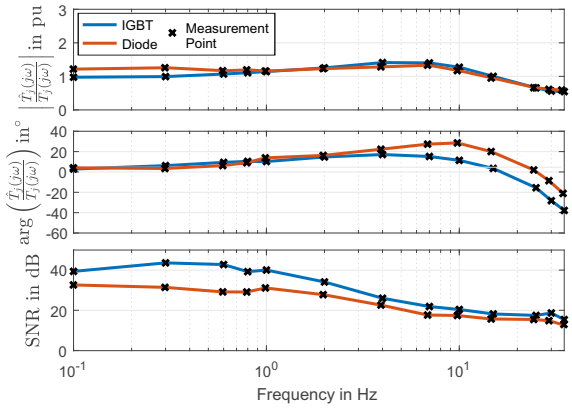

Fig. 11. Experimental characterization of the open loop EA

V. EXPERIMENTAL VALIDATION

A load emulator, whose topology is depicted in Fig. 9, was used to operate a decapsulated HP2 module and to test the observer under realistic operation conditions at a dc-link voltage of 100 V and with Ethylene-Glycol water coolant at a temperature of 20 °C. The observer structure was implemented in C++ on a Shark DSP from Analog Devices and operated with $f_{\mathrm{s}} = 1\,\mathrm{kHz}$ to monitor a HP2 module during operation. The computation frequency of the observer was selected to ensure that the DSP finishes all calculations each interrupt. The current control [25] was realized with a PWM frequency of 5 kHz to ensure that the current ripple remains small and does not effect the switching losses. The device temperature measurements were obtained from the decapsulated power module with four LT25F infrared sensors from Optris, which allow a sampling rate of 500 Hz and show a delay of 10 ms. The device under test on the test bench is depicted in Fig. 10.

First, the estimation accuracy of the open loop observer was determined experimentally to evaluate the electro-thermal real time model's suitability for the application. Therefore, multiple experiments have been conducted, operating the power module at one excitation frequency after another with constant current and voltage amplitude The observer was operated open loop, and the open loop estimates and the device temperature measurements were recorded. After the experiment, the thermal cycle amplitudes of the measurement and the estimates were determined using Fourier Analysis and related to each other. The resulting data points are depicted together with the signal to noise ratio (SNR) in Fig. 11, which is the open loop estimation accuracy plot. The result shows, that the open loop model exhibits a maximum error of 20 % up to 20 Hz. Above 20 Hz the signal to noise ratio is to low, making the extraction of the EA difficult. Finally, the observer structure is validated over a representative operation profile, as illustrated in Fig. 12. It can be seen that the junction temperature estimates nicely follows their measurements but reject most of the noise. Meanwhile, the spatial temperatures are extracted transiently and averaged. They allow accurate monitoring of the thermal stress at the most critical locations of the power module.

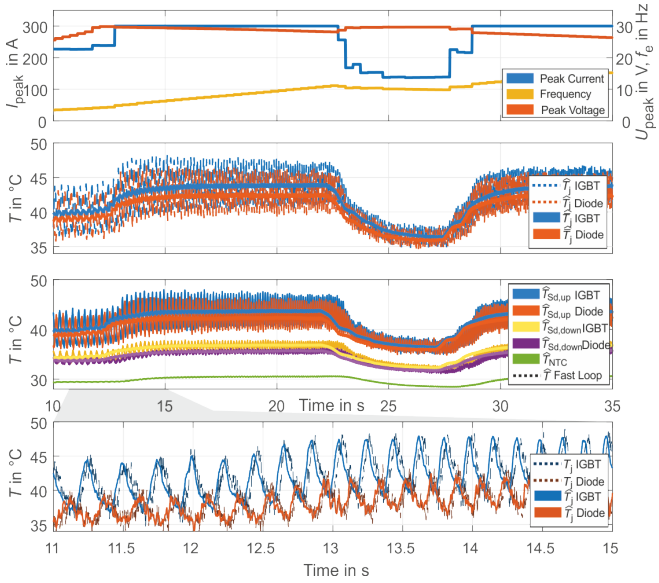

Fig. 12. Transient and averaged temperature estimation with the 3-D spatial observer over a realistic load profile

VI. Conclusion

It is shown in this work that observer based 3-D spatial temperature estimation with a reduced order finite difference model is feasible. The enhanced, cascaded Luenberger observer structure provides a framework to accurately estimate the transient and averaged temperature at various points of the power module. The structure appropriately uses a measured junction temperature signal, which is often superimposed with noise, and computes smooth estimates of junction and 3-D spatial temperatures with high bandwidth and nearly zero lag. In addition, it provides information which can be used to detect the degradation of the power module. The concept has been evaluated experimentally on a load emulator with realistic load profiles.

Acknowledgment

The work was supported by a research scholarship of the German Academic Exchange Service (DAAD).

References

[1] S. Yang, D. Xiang, A. Bryant, P. Mawby, L. Ran, and P. Tavner, "Condition monitoring for device reliability in power electronic converters: A review," *IEEE Transactions on Power Electronics*, vol. 25, no. 11, pp. 2734–2752, Nov. 2010.

[2] V. Blasko, R. Lukaszewski, and R. Sladky, "On line thermal model and thermal management strategy of a three phase voltage source inverter," in *Industry Applications Conference, 1999*, 1999.

[3] D. A. Murdock, J. E. R. Torres, J. J. Connors, and R. D. Lorenz, "Active thermal control of power electronic modules," *IEEE Transactions on Industry Applications*, vol. 42, no. 2, pp. 552–558, Mar. 2006.

[4] T. Polom, B. Wang, and R. D. Lorenz, "Control of junction temperature and its rate of change at thermal boundaries via precise loss manipulation," *IEEE Transactions on Industry Applications*, 2017.

[5] M. Andresen, M. Liserre, and G. Buticchi, "Review of active thermal and lifetime control techniques for power electronic modules," in *Power Electronics and Applications (EPE'14-ECCE Europe), 2014 16th European Conference on*, Aug. 2014, pp. 1–10.

[6] C. H. van der Broeck, L. A. Ruppert, R. D. Lorenz, and R. W. De Doncker, "Active thermal cycle reduction of power modules via gate resistance manipulation," in *Applied Power Electronics Conference and Exposition (APEC)*, 2018.

[7] D. C. Katsis and J. D. van Wyk, "Void-induced thermal impedance in power semiconductor modules: Some transient temperature effects," *IEEE Transactions on Industry Applications*, vol. 39, no. 5, pp. 1239–1246, Sep. 2003.

[8] M. Warwel, G. Wittler, M. Hirsch, and H. C. Reuss, "Real-time thermal monitoring of power semiconductors in power electronics using linear parameter-varying models for variable coolant flow situations," in *2014 IEEE 15th Workshop on Control and Modeling for Power Electronics (COMPEL)*, Jun. 2014, pp. 1–6.

[9] X. Wang, A. Castellazzi, and P. Zanchetta, "Full-order observer based igbt temperature online estimation," in *IECON 2014 - 40th Annual Conference of the IEEE Industrial Electronics Society*, Oct. 2014, pp. 1494–1498.

[10] M. A. Eleffendi and C. M. Johnson, "Application of kalman filter to estimate junction temperature in igbt power modules," *IEEE Transactions on Power Electronics*, vol. 31, no. 2, pp. 1576–1587, Feb. 2016.

[11] M. Andresen, M. Schloh, G. Buticchi, and M. Liserre, "Computational light junction temperature estimator for active thermal control," in *2016 IEEE Energy Conversion Congress and Exposition (ECCE)*, 2016.

[12] M. A. Eleffendi and C. M. Johnson, "In-service diagnostics for wire-bond lift-off and solder fatigue of power semiconductor packages," *IEEE Transactions on Power Electronics*, vol. 32, no. 9, pp. 7187–7198, Sep. 2017.

[13] C. H. van der Broeck, M. Conrad, and R. De Doncker, "A thermal modeling methodology for power semiconductor modules," *Microelectronics Reliability*, vol. 55, no. 9-10, pp. 1938–1944, 2015.

[14] C. H. van der Broeck, L. A. Ruppert, A. Hinz, M. Conrad, and R. W. de Doncker, "Spatial electro-thermal modeling and simulation of power electronic modules," *IEEE Transactions on Industry Applications*, vol. PP, no. 99, pp. 1–1, 2017.

[15] C. H. van der Broeck, L. A. Ruppert, and R. De Doncker, "Spatial electro-thermal modeling and simulation of power electronic modules," in *IEEE Energy Conversion Congress and Exposition*, 2016.

[16] R. Goldbeck, C. H. van der Broeck, and R. W. D. Doncker, "Electro-thermal simulation of bond wires in power modules for realistic mission profiles," in *12th IEEE International Conference on Power Electronics and Drive Systems (PEDS 2017)*, 2017.

[17] B. Moore, "Principal component analysis in linear systems: Controllability, observability, and model reduction," *Automatic Control, IEEE Transactions on*, vol. 26, no. 1, pp. 17–32, Feb. 1981.

[18] R. C. Dorf and R. H. Bishop, *Modern control systems*, 9th. Upper Saddle River, NJ, USA: Prentice-Hall, Inc., 2000.

[19] J. Gottschlich, M. Kaymak, M. Christoph, and R. De Doncker, "A flexible test bench for power semiconductor switching loss measurements," in *11th International Conference on Power Electronics and Drive Systems*, Jun. 2015, pp. 442–448.

[20] G. Engelmann, M. Laumen, K. Oberdieck, and R. W. De Doncker, "Modular tempering unit for device characterization in a double pulse test bench," in *17th International Conference on Power Electronics and Motion Control*, Sep. 2016.

[21] M. Wolf, H. d. T. Mouton, J. W. van der Merwe, and F. Koeslag, "An investigation of switching and conduction losses in inverters under varying inductor ripple current," in *AFRICON 2009*, 2009.

[22] E. R. Motto and J. F. Donlon, "Igbt module with user accessible on-chip current and temperature sensors," in *2012 Twenty-Seventh Annual IEEE Applied Power Electronics Conference and Exposition (APEC)*, Feb. 2012, pp. 176–181.

[23] C. H. van der Broeck, A. Gospodinov, and D. D. ; W., "Igbt junction temperature estimation via gatevoltage plateau sensing," in *IEEE Energy Conversion Congress and Exposition*, 2017.

[24] H. Niu and R. D. Lorenz, "Sensing igbt junction temperature using gate drive output transient properties," in *2015 IEEE Applied Power Electronics Conference and Exposition (APEC)*, Mar. 2015, pp. 2492–2499.

[25] C. H. van der Broeck, R. W. D. Doncker, S. A. Richter, and J. von Bloh, "Discrete time modeling, implementation and design of current controllers," in *IEEE Energy Conversion Congress and Exposition*, Sep. 2014, pp. 540–547.